Diffusion on random-site percolation clusters: Theory and NMR microscopy experiments with model objects

Andreas Klemm,[1] Ralf Metzler,[2] and Rainer Kimmich[1]

[1]*Sektion Kernresonanzspektroskopie, Universität Ulm, 89069 Ulm, Germany*

[2]*Department of Physics, Massachusetts Institute of Technology, 77 Massachusetts Avenue, Room 12-109, Cambridge, Massachusetts 02139*

Quasi-two-dimensional random-site percolation model objects were fabricated based on computer-generated templates. Samples consisting of two compartments, a reservoir of H_2O gel attached to a percolation model object, which was initially filled with D_2O, were examined with nuclear magnetic resonance microscopy for rendering proton spin density maps. The propagating proton/deuteron interdiffusion profiles were recorded and evaluated with respect to anomalous diffusion parameters. The deviation of the concentration profiles from those expected for unobstructed diffusion directly reflects the anomaly of the propagator for diffusion on a percolation cluster. The fractal dimension of the random walk d_w evaluated from the diffusion measurements on the one hand and the fractal dimension d_f deduced from the spin density map of the percolation object on the other permits one to experimentally compare dynamical and static exponents. Approximate calculations of the propagator are given on the basis of the fractional diffusion equation. Furthermore, the ordinary diffusion equation was solved numerically for the corresponding initial and boundary conditions for comparison. The anomalous diffusion constant was evaluated and is compared to the Brownian case. Some *ad hoc* correction of the propagator is shown to pay tribute to the finiteness of the system. In this way, anomalous solutions of the fractional diffusion equation could experimentally be verified.

I. INTRODUCTION

Randomly disordered media are present in many fields of nature and science. The dynamical properties ruled by the geometrical structure are of special interest in fields of physical and engineering processes, such as filtering and exploration of fossil fuels [1–3]. Percolation theory has proven to be a powerful tool to model porous systems [4–6].

The objective of this study is to examine diffusion on random-site percolation clusters experimentally and analytically. There are several numerical simulation studies in the literature suggesting an anomalous displacement behavior related to the fractal nature of the clusters [7–9]. However, there is little experimental evidence for the reality and practical detectability of anomalous diffusion so far [10–12].

The objective of the present work is to exploit a different experimental strategy. This is (a) to generate numerically a percolation cluster, (b) to determine the characteristic parameters numerically, (c) to fabricate model objects using the percolation clusters as templates, (d) to record nuclear magnetic resonance (NMR) spin density maps from the (water-filled) pore space, (e) to evaluate the characteristic cluster parameters on this basis again, (f) to study interdiffusion of heavy and light water in the pore space, and (g) to compare the experimental interdiffusion profiles with solutions of the fractional diffusion equation [13]. In a sense, we are thus continuing our previous work in which we had already explored static and dynamic properties in various three-dimensional and quasi-two-dimensional percolation model objects [14–17].

Random-site percolation structures are defined in the two-dimensional case by sites on a square lattice. They are occupied with a probability p that is usually chosen in the vicinity of the (two-dimensional) percolation threshold [4] $p_c = 0.592\,746$. Neighboring occupied sites are connected by pores with a cross section corresponding to the lattice constant or integer multiples of it. The total subset of connected lattice sites form a so-called cluster. For $p \geqslant p_c$, sample-spanning clusters occur that can be examined with respect to transport properties. The pore space structure generated by the random-site percolation model can be characterized by four parameters, that is, the lattice constant a, the fractal dimension d_f, the correlation length ξ, and the percolation probability P_∞ [4,6,18]. The latter quantity is defined as the probability that a site belongs to the ''infinite'' cluster traversing the whole sample [19]. The correlation length, which is of particular interest here, is defined as the mean distance between two sites of a finite cluster (or the mean hole diameter in an infinite cluster). In the real percolation model objects we are considering here, the minimum lattice constant (or pore diameter) is given by the mechanical resolution of the fabrication process (see below).

Random-site percolation clusters are known to display fractal properties on a length scale below the correlation length. That is, the volume-averaged porosity scales with the probe volume radius r_p as

$$\rho \propto \begin{cases} r_p^{d_f - d_E} & \text{for } a \ll r_p \ll \xi \\ P_\infty \propto r_p^0 & \text{for } r_p \gg \xi. \end{cases} \quad (1)$$

The Euclidean dimension is denoted by d_E (equals 2 in the present case). The fractal dimension for $d_E = 2$ was theoretically derived as $d_f = 91/48 \approx 1.896$ [4].

The purely structural relationship Eq. (1) is in juxtaposition to the dynamic property for the mean squared displacement of a random walker on the cluster

$$\langle r_d^2 \rangle \propto \begin{cases} t^{2/d_w} & \text{for } t_a \ll t \ll t_\xi \\ D_{\text{eff}} t & \text{for } t \gg t_\xi, \end{cases} \qquad (2)$$

where $t_\xi \propto \xi^{d_w}$ is the time the random walker needs to explore the correlation length ξ, and d_w is the fractal dimension of the random walk. The lower time limit of the anomalous diffusion regime is given by the time needed for the displacement of length a, t_a. The diffusion coefficient becoming effective in the long-time limit $t \gg t_\xi$ is denoted by D_{eff}. According to the Alexander-Orbach conjecture [20], the quantity d_w is assumed to be related to the fractal cluster dimension as

$$d_w = \tfrac{3}{2} d_f \quad \text{for} \quad d_E \geqslant 2. \qquad (3)$$

That is the structural parameter d_f characteristic of the volume-averaged porosity is linked to the dynamic parameter d_w specifying anomalous diffusion. For $d_E = 2$, the diffusion exponent becomes $d_w \approx 2.87$. In this study experimental evaluations for both quantities have been carried out, so that a comparison becomes possible. Note, however, that Eq. (3) is not considered to be an exact relation [4,6,21,22].

A theoretical problem of intriguing impact is the complete propagator description of anomalous diffusion rather than restricting oneself to the second moment of the propagator according to Eq. (2). In the second part of this paper, the analytical treatment based on the fractional diffusion equation [13,23] is outlined and compared with the interdiffusion profile data acquired in our experiments.

II. TECHNIQUES AND INSTRUMENTS

A. Methods for measuring diffusion

In the model objects to be studied here, the minimum pore diameter is $\Delta r = 400 \, \mu$m. The displacement length scale needed to probe anomalous diffusion, i.e., displacements obstructed by the matrix, is $r_d \gg \Delta r$. The ordinary pulsed-gradient spin echo technique (see Refs. [24], [25], for instance) is therefore not suitable for the detection of anomalies in liquids in the present situation.

The much larger displacement rate in gaseous phases would permit such studies in principle. In Ref. [15] we have studied diffusion of methane gas in a percolation model object. Although there was some indication of an anomalous behavior, the experiment turned out to be difficult due to the poor detection sensitivity. In this respect, diffusion studies using laser-polarized or thermally polarized ^{129}Xe are more promising [26,27]. Also, the use of inert fluorinated gases possibly at somewhat elevated pressures may be more favorable [28,29]. In any case, there is a diffusion mechanism (Knudsen diffusion) relevant in gases, which is different by nature from the diffusion in liquids [8].

We, therefore, preferred to employ an isotope interdiffusion method. The samples consisted of two compartments initially filled with H_2O (in gel form) and D_2O. At the beginning of the experiment the compartments were pressed on each other in close contact so that interdiffusion was initiated. The time evolution of the proton spin density maps in the D_2O compartment was then studied as a function of the

time. The technique was ordinary one- or two-dimensional NMR imaging of concentration profiles, an application for diffusometry purposes already described in Refs. [30–32].

The proton density profiles were recorded either in the form of one-dimensional spin density maps, or were evaluated from the two-dimensional spin density maps by projection on the main diffusion direction. The latter variant has the advantage that the signal noise from matrix areas can be screened off before evaluating the profile data.

The propagation of the proton density profile at half-height as a function of the time permits one to determine the time dependence of the mean squared displacements. Alternatively, the profiles themselves at a given time can be examined with respect to the character of the diffusion process. In the latter case, the full propagator characteristics, and not just its second moment, are mattering.

B. NMR tomograph and acquisition parameters

The one- or two-dimensional proton density maps of the water-filled pore space of percolation model objects were recorded with the aid of a NMR tomograph consisting of a 4.7-T Bruker magnet with 40 cm horizontal room temperature bore and a home made radio frequency console. Typical radio frequency and field gradient pulse schemes for spin-echo NMR imaging can be found in Ref. [24], for instance. The spatial resolution of the images was better than 300 μm. The acquisition of a two-dimensional spin density map typically took $20' - 60'$, so that a reasonable time resolution was given.

Isotopic dilution by deuterons prolongs the local transverse and longitudinal relaxation times due to the reduced number of dipolar interaction partners (see Ref. [33], for instance). For the evaluation of spin density maps, the spin-echo signals therefore have to be corrected if the repetition time is not much longer than the longest proton spin-lattice relaxation time T_1 or if the echo time is not much shorter than the transverse relaxation time T_2.

Typical echo times T_E were between 20 and 30 ms. This is to be compared with transverse relaxation times of several seconds in water at room temperature. Signal attenuation on this basis is, therefore, totally negligible.

The situation is less clear with the effect of spin-lattice relaxation. The repetition time T_R typically was 2 s, so that the spin density profiles could be distorted at the low-concentration side by saturation effects. In some of the experiments, we have, therefore, varied the repetition time between 0.25 and 12.2 s in order to evaluate the local spin-lattice relaxation times. The local signal intensities were then corrected correspondingly to provide the true spin density profiles. No significant spin-lattice relaxation effect could be diagnosed (see the data discussed below).

C. Computer generated percolation clusters

In the insets of Figs. 6 and 8, typical two-dimensional random-site percolation clusters generated on a square lattice are shown. The occupation probability p is slightly above the percolation threshold value $p_c = 0.5927$ for the Euclidean dimension $d_E = 2$ [34]. The volume-averaged porosity was
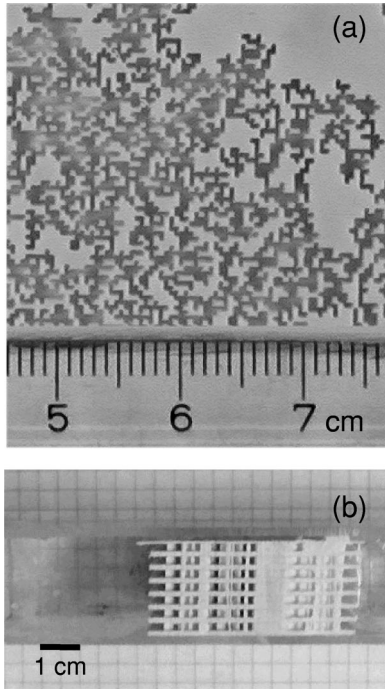
FIG. 1. Photograph of a section of a quasi-two-dimensional random-site percolation model object (top view) (a) and of an entire model object (cross section) (b). The model object consists of several identical quasi-two-dimensional percolation clusters stacked on each other in order to improve the signal intensity. The mechanical resolution of the fabrication process was 400 μm. The adjusted milling depth was constant between 1 to 2 mm in the various objects produced.

evaluated using the so-called sandbox method [14,15]: N_p probe circles of varying radius r_p are first placed at positions $\mathbf{r_k}$ within the cluster in such a way that the center of the probe volume (which actually is an area in the two-dimensional case) is in the pore space. Then the average values of the observables are formed for the N_V voxels at positions $\mathbf{r_j}$ inside the probe volume. Finally, the arithmetic mean of the data set for the N_p probe volumes with a given radius r_p is taken. In other words, the volume-averaged porosity is defined as

$$\rho(r_p) = \frac{1}{N_p} \sum_{k=1}^{N_p} \frac{1}{N_V} \sum_{j=1}^{N_V} \rho(\mathbf{r_j}), \qquad (4)$$

where $r \geq |\mathbf{r_k} - \mathbf{r_j}|$. This quantity can also be evaluated from black-and-white converted, experimental spin density maps as described in Ref. [14].

D. Model objects and measuring conditions

The percolation model objects were fabricated using a circuit board plotter (for details see Refs. [14–16]) based on the computer-generated templates. The mechanical fabrication resolution was $\Delta r = 400$ μm (see photograph in Fig. 1). The adjusted milling depth ranged from 1 to 2 mm in the different objects produced.

The objects were filled with heavy water and brought into contact with reservoirs of H_2O gel (Kelcogel, 1.5% by weight) at time $t = 0$, when the interdiffusion process was to begin. The reservoirs are schematically shown in the insets of Figs. 6 and 8. The proton distribution in the objects was then measured as a function of the time in the form of spin density maps as described above.

The gel form of the undeuterated moiety of the sample was needed for stabilization and to prevent flow. On the other hand, gel stabilization inside the percolation matrix is unfavorable owing to the tendency of forming voids upon gelation. It turned out that in this case the stabilizing effect of the solid matrix is sufficient.

The influence of deuteration and gelation on the bulk water self-diffusion coefficient was checked in an ordinary pulsed-gradient spin-echo experiment [24]. At 20 °C and a gel content of 1.2%, the self-diffusion coefficients of H_2O and D_2O were found to be 1.8×10^{-9} and 1.4×10^{-9} m^2/s, respectively. That is, the water self-diffusion coefficient is slightly reduced both by deuteration and gelation.

An isotope effect is known to show up already without gelation: Mills [35] reports self diffusion coefficients in pure H_2O and D_2O at 25 °C $D_{H_2O} = 2.3 \times 10^{-9}$ and $D_{D_2O} = 1.87 \times 10^{-9}$ m^2/s, respectively. That is, smaller diffusion coefficients are expected with increasing dilution of ^{1}H as it occurs at the diffusion front.

Furthermore, there may be a difference in the chemical potential in pure H_2O and pure D_2O, so that a slight deviation from the self-diffusion situation may play a role. On the other hand, no significant influence on the shape and time evolution of the interdiffusion profiles was found in the bulk-to-bulk experiments described below. The conclusion, therefore, is that all these effects are of minor importance or largely compensate each other so that (partial) deuteration and gelation does not perceptibly affect the percolation cluster characteristics of the propagator to be probed.

The quasi-two-dimensional model objects were kept in a horizontal position during the whole measuring process in order to avoid any convective displacements. In order to improve the detection sensitivity, several identical slices were stacked on each other (see Fig. 1). All experiments were carried out at room temperature, (21 ± 1) °C.

III. RESULTS

A. Volume-averaged porosity

The volume-averaged porosity was evaluated as a function of the probe volume radius on the basis of Eq. (4) for the percolation clusters shown in the insets of Figs. 6 and 8. Corresponding evaluations for experimental spin density maps lead to equivalent decays as demonstrated in Ref. [17]. The fractal dimension according to Eq. (1) was found to be $d_f = 1.87$ in both cases. This value will be compared with the experimental value for d_w according to Eq. (3).

B. Isotope concentration profiles for interdiffusion between bulk water compartments

In order to test our measuring and evaluation technique, we have recorded isotopic interdiffusion profiles in a sample

consisting of two equal compartments initially filled with bulk H_2O and D_2O gels, respectively. In this case, the initial distribution of the proton density is of the type

$$C(x,t=0) = \begin{cases} C_0 & \text{for } x \leq 0 \\ 0 & \text{for } x > 0. \end{cases} \qquad (5)$$

Provided that the diffusion process is normal, that is, in the absence of obstructions by a matrix, the proton spin density profiles at later times are given by [36]

$$C(x,t) = \frac{1}{2} C_0 \, \text{erfc}\left\{ \frac{x}{2\sqrt{Dt}} \right\}, \qquad (6)$$

where D is the diffusion coefficient and $\text{erfc}(z)$ is the complementary error function. In principle, this solution of the ordinary diffusion equation applies to "infinite" systems, that is, to root mean squared displacements much less than the extension of the sample.

Figure 2 shows experimental proton spin density maps measured in a two-compartment sample (for an illustration see inset of Fig. 3) as a function of the time t after bringing the compartments into contact with each other. The right and left compartments were initially filled with bulk H_2O and D_2O gels, respectively. The mean proton spin density profiles, i.e., projections of the two-dimensional spin density maps on the main diffusion coordinate axis x are also shown in diagram form (white lines).

In Fig. 3, these experimental concentration profiles are compared with those predicted by Eq. (6). The fits of Eq. (6) to the experimental data reproduces the room temperature value of the diffusion coefficient measured in bulk water with the pulsed-gradient spin-echo technique [35,37], $D = 2 \times 10^{-9}$ m^2/s, very well with the exception of the shortest and longest diffusion intervals.

At the shortest diffusion interval, imperfections of the initial isotope distribution and the limited time resolution of the (two-dimensional imaging process) are expected to matter. The concentration profiles at the longest diffusion times are already affected by the finite extension of the sample, which conflicts with the assumption in Eq. (6) of infinite compartments.

Taking together the potential sources of systematic experimental errors mentioned before, one can state that the agreement between the theoretical and experimental concentration profiles in bulk samples is very reasonable so that reliable evaluations of anomalous diffusion features in the percolation model objects can be expected. This is corroborated by the determination of the mean square displacement of the diffusion front in a second experiment. The setup is schematically shown in the inset of Fig. 4. In this case, the half-height positions of the concentration profiles (projections of the two-dimensional spin density maps on the main diffusion direction) were evaluated, squared, and plotted versus time.

The middle section of the experimental curve shown in Fig. 4 can nicely be described by a power law $x_{1/2}^2 \propto t^{1.05}$, which is very close to the linear mean squared displacement law for normal diffusion. As in the experiment discussed before, the deviations at short times reflect the initial situa-
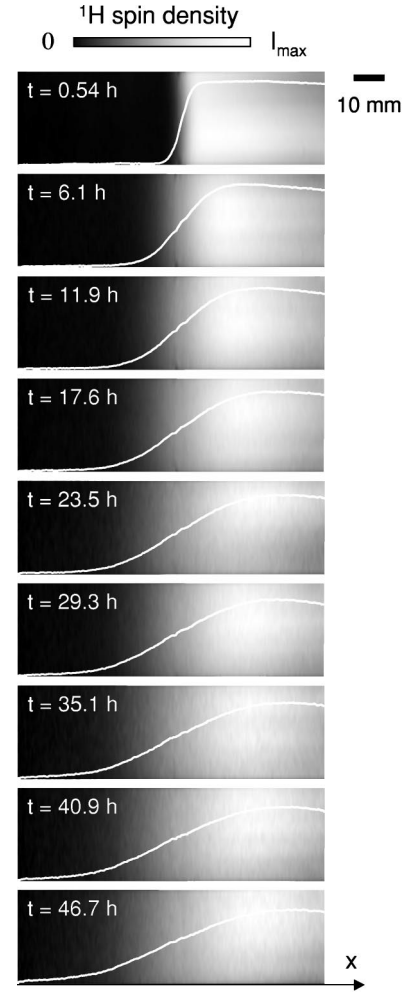

FIG. 2. Proton spin density maps recorded in a two-compartment sample initially filled with bulk H_2O and D_2O gels (see the inset picture in Fig. 3). The echo time was $T_E = 28$ ms, the repetition time was $T_R = 2$ s. The field of view in x direction was 15 cm. The digital resolution was 290 μm. The times indicate the span after contacting the two gels. The white lines represent the isotopic interdiffusion profiles in the form of the projection of the proton spin density on the x direction.

tion that can only imperfectly be described by a step function. The plateau reached at long times is due to the finite extension of the sample.

C. Isotope concentration profiles for interdiffusion between bulk water and water-filled percolation cluster compartments

Equation (6) is based on a Gaussian propagator as expected for ordinary diffusion. That is, it does not account for diffusion in a percolation cluster where the second moment of the propagator obeys an anomalous diffusion law as given in Eq. (2).

Figure 5 shows two-dimensional proton spin density maps acquired in an experimental setup schematically shown in the inset of Fig. 6. Interdiffusion between a H_2O gel filled reservoir and a stack of quasi-two-dimensional percolation
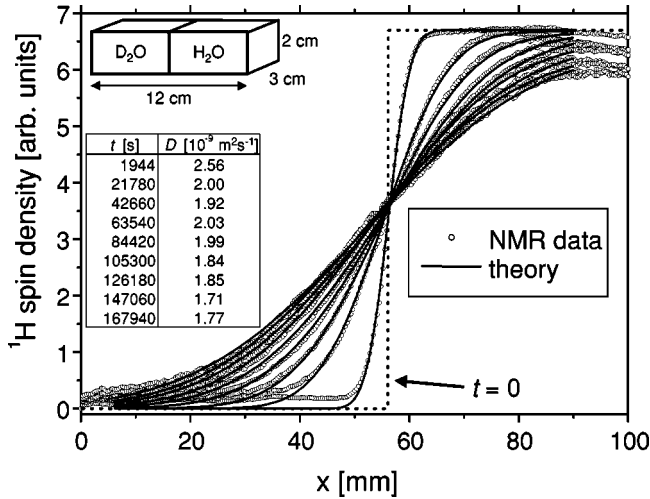
FIG. 3. Comparison of theoretical and experimental interdiffusion profiles between bulk H_2O and D_2O gels. The data correspond to the two-dimensional spin density maps shown in Fig. 2. The solid lines represent fits of Eq. (6) to the experimental data. The fitted diffusion coefficients are given in the inset table.

model objects was examined. Superimposed on to the spin density maps the mean spin density profiles (i.e., projections on the x axis) are shown in Fig. 5 as white lines.

The half-height positions of these mean concentration profiles $x_{1/2}$ were evaluated, squared, and plotted versus time as shown in Fig. 6. In the limit of long diffusion times when the imperfections of the initial isotope distribution and the finite time resolution of $26'$ do not matter anymore, the data can be described by a power law again. The imperfection of
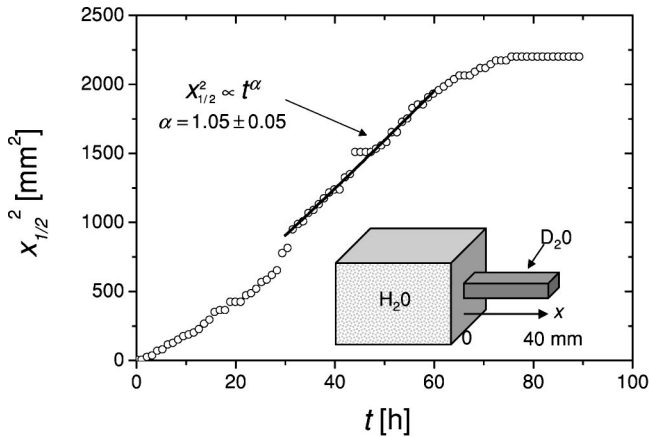

FIG. 4. Square of the position of the proton concentration profile at half-height in bulk versus diffusion time. The experimental setup consisted of two compartments initially filled with bulk H_2O and D_2O gels as shown in the inset picture. The largely asymmetric sizes of the H_2O and D_2O reservoirs ensure a practically constant proton concentration at the entrance of the D_2O compartment. The cross section of the D_2O compartment was 1.5×2 cm^2. The concentration profiles were obtained as projections of two-dimensional spin density maps on the x axis. The spin-echo time was $T_E = 32$ ms, the repetition time was $T_R = 0.7$ s. The field of view in x direction was 7 cm. A digital resolution of 270 μm was adjusted. The total acquisition time for a spin density map was 1 h.

the initial isotope distribution is matched by the revised origin of time t. Fitting the exponent of Eq. (2) for $t \ll t_\xi$ to the data leads to $d_w = 2.89$, which favorably compares to the Alexander-Orbach conjecture, Eq. (3), with the fractal dimension d_f determined from the very same percolation cluster according to Eq. (1) for $a \ll r_p \ll \xi$.

The isotopic interdiffusion profiles can also be obtained directly with the aid of one-dimensional imaging along the main diffusion direction. Figure 7 renders typical profiles recorded in this way from an experimental setup schematically shown in the inset of Fig. 8. The data are corrected for saturation effects due to incomplete spin-lattice relaxation after the repetition interval. From these profiles, the mean squared proton displacement (in the percolation cluster moiety) can be evaluated as a function of the diffusion time. Figure 8 shows corresponding data. Details are described in the legend. With a fitted exponent parameter of $d_w = 2.86$ the anomalous diffusion character in the percolation cluster is again corroborated in good agreement with the Alexander Orbach conjecture Eq. (3).

IV. ANALYTICAL PROPAGATOR TREATMENT BASED ON THE FRACTIONAL DIFFUSION EQUATION

The propagator (or Green's function) for a Brownian random walk process in one dimension is, of necessity, given in terms of the Gaussian

$$C(x,\tau) = \frac{1}{\sqrt{4\pi\tau}} \exp\left(-\frac{x^2}{4\tau}\right), \qquad (7)$$

due to the central limit theorem [38]. Expression (7) includes the δ-initial condition $C(x,0) = \delta(x)$ and fulfills natural boundary conditions $\lim_{|x| \to \infty} C(x,t) = 0$. We use the rescaled time $\tau \equiv Dt$. The propagator (7) satisfies the diffusion equation [38]

$$\frac{\partial}{\partial \tau} C = \frac{\partial^2}{\partial x^2} C(x,\tau). \qquad (8)$$

Representing the experimental setup shown in the inset of Fig. 4 by the initial condition $C(x,0) = 0$ for $x > 0$ and through the boundary condition $C(0,\tau) = C_0$, we assume that, due to the comparatively large reservoir, a constant concentration is kept at the boundary $x = 0$. The solution of Eq. (8) for these initial and boundary conditions is given through

$$C(x,\tau) = C_0 \, \text{erfc}\left(\frac{x}{2\sqrt{\tau}}\right), \quad x > 0. \qquad (9)$$

The solution given in Eq. (9) reaches the plateau $C(x,\tau) = C_0$ for $x^2 \ll \tau$. Consequently, the expression in Eq. (9) is not normalized. Its mean

$$\langle 1(\tau) \rangle \equiv \int_0^\infty C(x,\tau) dx = 2C_0 \sqrt{\tau/\pi}. \qquad (10)$$

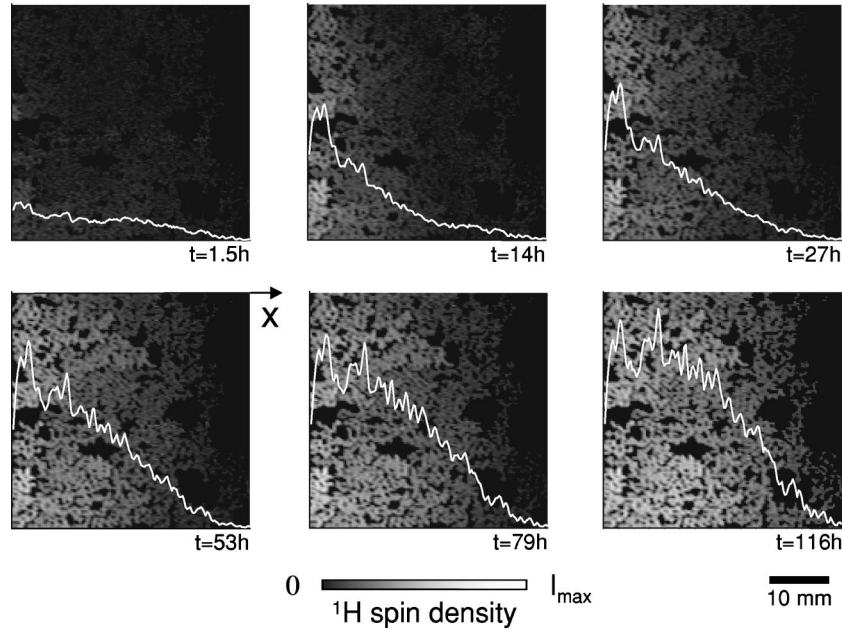grows with the square root in time, and is proportional to the concentration C_0. The second moment becomes

FIG. 5. Evolution of two-dimensional proton spin density maps (256×256 pixels) in a random-site percolation object. The experimental setup is schematically shown in the inset of Fig. 6. The times indicate the spans after attaching the H_2O gel compartment to the multistack percolation model object (matrix size 100×100; $p - p_c = 0.029$; $d_f = 1.87$, porosity of the percolating cluster $\rho = 0.5352$). The time resolution given by the image acquisition time was $26'$. The echo time was $T_E = 23$ ms, the repetition time was $T_R = 0.7$ s. The digital resolution of the maps is 230 μm. The white lines overlaid to the spin density maps represent the mean proton concentration profiles (projections of the diffusion front on the main diffusion direction).
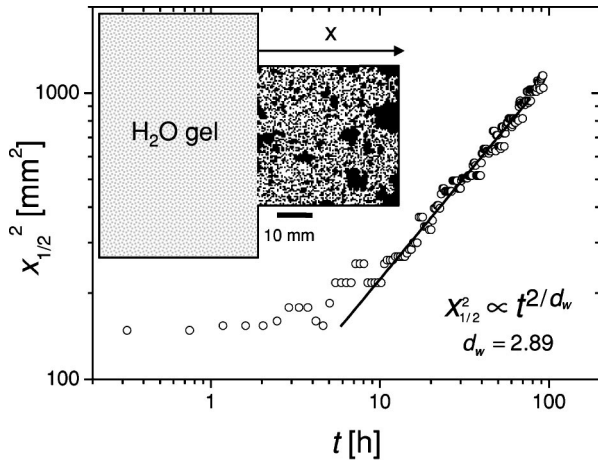

FIG. 6. Square of the position of the proton concentration profile at half-height in the percolation cluster shown and described in Fig. 5 versus diffusion time. The inset shows the experimental setup, where the percolation cluster (white) initially is filled with D_2O. The largely asymmetric sizes of the H_2O and D_2O reservoirs ensure a practically constant proton concentration at the entrance of the D_2O compartment, i.e., the percolation cluster. The concentration profiles were obtained as projections of two-dimensional spin density maps on the x axis (see Fig. 5). The time resolution is $26'$. The solid lines represent a fit of Eq. (2) for $t \ll t_\xi$. The fitted exponent parameter is $d_w = 2.89$.
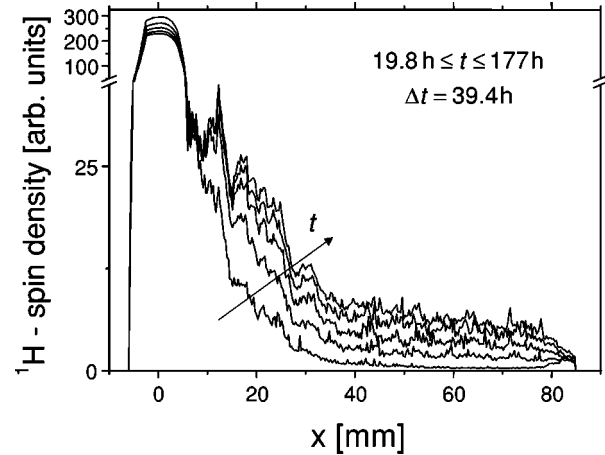

FIG. 7. Typical isotopic interdiffusion profiles directly measured with the aid of one-dimensional imaging along the main diffusion direction. The experimental setup is schematically shown in the inset of Fig. 8. The spin-lattice relaxation time $T_1(x)$ was measured as a function of x by varying the repetition time T_R from 0.2 to 12.2 s in 15 steps. The signal intensity profiles were then corrected by multiplication with a factor $(1 - \exp[T_R/T_1(x)])^{-1}$, so that any spatially dependent saturation effects were eliminated. The spin-echo time was 20 ms and the field of view along the x direction was 15 cm. A diffusion time resolution of 1 h, and a digital space resolution of 290 μm were adjusted.
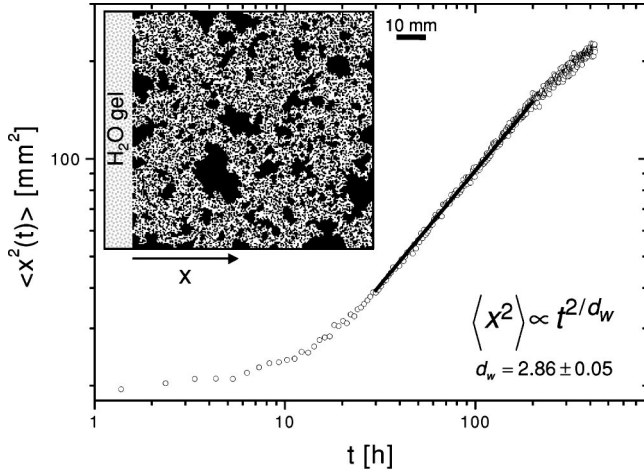
FIG. 8. Mean squared proton displacement as a function of the diffusion time in a two-dimensional random-site percolation object, the template of which is shown in the inset. The percolation cluster is initially ($t=0$) filled with D_2O. The characteristic data of the percolation cluster are: matrix size 200×200; occupation probability relative to the threshold value $p-p_c=0.030$; fractal dimension $d_f=1.87$; porosity of the percolating cluster $\rho=0.4845$. The mean squared displacement data were evaluated from proton concentration profiles recorded in the form of one-dimensional NMR images along the x axis. The proton concentration profiles were used to calculate the mean squared proton displacement in the percolation cluster moiety. The solid line represents a fit of Eq. (2) for $t\ll t_\xi$. The fitted exponent parameter is $d_w=2.86$.

$$\langle x^2(\tau)\rangle = \tfrac{8}{3}C_0\tau^{3/2}/\sqrt{\pi}. \tag{11}$$

In normalized form, that is, when the concentration profiles are divided by the mean given in Eq. (10), the mean squared displacement corresponds to

$$\langle x^2(\tau)\rangle_n = \frac{\langle x^2(\tau)\rangle}{\langle 1(\tau)\rangle} = \frac{4}{3}\tau. \tag{12}$$

It should be noted that the concentration profile $C(x,\tau)$ for the different realization with an infinite reservoir Eq. (6) differs from the case with constant boundary concentration Eq. (9) only by a factor $\frac{1}{2}$. Systems with constant boundary concentration and infinite reservoir thus behave congruently.

Let us now address how we can derive the analogous quantities for the anomalous diffusion data described in Sec. III C. As mentioned above, the average diffusion in the percolation cluster close to the percolation threshold is anomalous in the sense that the mean squared displacement follows $\langle x^2(\tau)\rangle\propto\tau^\alpha$, where $\alpha=2/d_w$ [see Eq. (2)], and $d_w=2d_f/d_s$ [9,39]. Here, the rescaled time $\tau=(D_\alpha)^{1/\alpha}t$ includes the anomalous diffusion constant D_α of dimension $[D_\alpha]=m^2/s^\alpha$ [13,40]. Thus, the diffusion dynamics is controlled by two parameters, the fractal dimension d_f and the spectral dimension d_s. Usually, the inequality $d_w>d_f$ is fulfilled so that the anomalous diffusion process is subdiffusive, i.e., $0<\alpha<1$. In the experiment, the three-dimensional probability density function is projected onto a one-dimensional prob-

ability density function, and therefore the geometry in the pseudo-one-dimensional process becomes averaged.

In the original geometry, the spreading of the random walker in space is slowed down in comparison to the free diffusion, due to the presence of bottlenecks and dead ends on all length scales, leading to the subdiffusive nature of the mean squared displacement. In the projection, the trapping in a small pore of the percolation cluster corresponds to a small wiggling around some given coordinate. Effectively, the walker in the pseudo-one-dimensional measurement experiences a continued multiple trapping process, i.e., it is immobilized for some "time" span τ governed by the so-called waiting "time" distribution $\psi(\tau)$. According to this ψ, the walker is released and moves freely until it is trapped again. This is a special case of a continuous time random walk process, the subdiffusion being reflected in the inverse power-law form $\psi(\tau)\sim A_a\tau^{-1-\alpha}$ [42]. According to this ψ, the walker is released and moves freely until it is trapped again, and so forth. This stop-and-go process can be mapped onto the fractional diffusion equation [13,23]

$$\frac{\partial}{\partial\tau}C = {}_0\mathcal{D}_\tau^{1-\alpha}\frac{\partial^2}{\partial x^2}C(x,\tau) \tag{13}$$

that includes the Riemann-Liouville fractional operator ${}_0\mathcal{D}_\tau^{1-\alpha}\equiv\partial/\partial\tau({}_0\mathcal{D}_\tau^{-\alpha})$ with [43]

$$_0\mathcal{D}_\tau^{-\alpha}C(x,\tau)\equiv\frac{1}{\Gamma(\alpha)}\int_0^\tau d\tau'\frac{C(x,\tau')}{(\tau-\tau')^{1-\alpha}} \tag{14}$$

The fractional diffusion equation is equivalent to a generalized master equation, and can be derived from a multiple trapping version of the fundamental Chapman-Kolmogorov equation [44].

The Riemann-Liouville operator has the important property that its Laplace transform is $\int_0^\infty e^{-u\tau}{}_0\mathcal{D}_\tau^{-\alpha}f(\tau)d\tau=u^{-\alpha}f(u)$. By virtue of this property, it can be shown that in Laplace space, the solution of the fractional diffusion equation, let us call it $C_\alpha(x,\tau)$, is connected to the solution
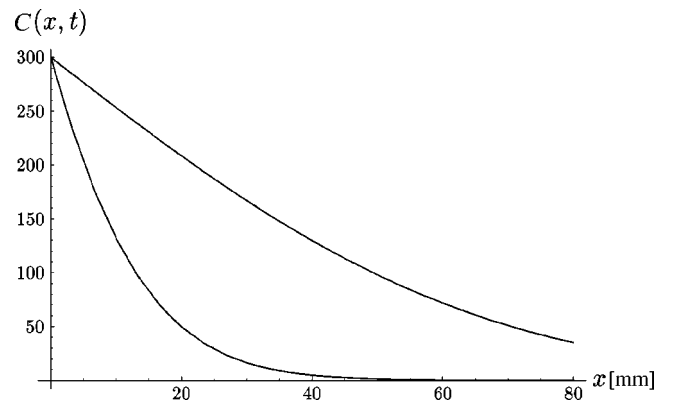

FIG. 9. Comparison between the anomalous concentration profile $C_{2/3}(x,\tau)$, left, and its Brownian analog $C_1(x,\tau)$, for a diffusion time interval $t=180$ h. We used $D_{2/3}=1.3\times10^{-8}$ $m^2/s^{2/3}$ and $D=2\times10^{-9}$ m^2/s. The amplitude is $C_0=300$ in both cases. The Brownian profile shows the much more efficient spread of the tracer substance into the medium.

of the Brownian diffusion equation (8), $C_B(x,\tau)$, through the scaling relation $C_\alpha(x,u) = u^{\alpha-1}C_B(x,u^\alpha)$ [13]. This, in turn, can be used to find a convenient mapping between the Brownian solution, and any quantity obtained from it through linear operations, in terms of the generalized Laplace transformation [45]

$$C_\alpha(x,\tau) = \int_0^\infty E_\alpha(s,\tau)C_B(x,s)ds. \qquad (15)$$

In Eq. (15), the function $E_\alpha(s,\tau)$ is a one-sided Lévy distribution that can be represented in terms of Fox's H function [13]. For our purposes, we notice that E_α has the convenient representation

$$E_{2/3}(s,\tau) = \frac{1}{\tau^{2/3}\Gamma(1/3)} \,_1F_1\left(\frac{5}{6};\frac{2}{3};-\frac{4s^3}{27\tau^2}\right)$$
$$- \frac{1}{\tau^{4/3}\Gamma(-1/3)} \,_1F_1\left(\frac{7}{6};\frac{4}{3};-\frac{4s^3}{27\tau^2}\right) \qquad (16)$$

for $\alpha = \frac{2}{3}$. This value for α is sufficiently close to the percolation cluster value 0.7, and we choose $\frac{2}{3}$ as for this rational number the representation in Eq. (16) considerably reduces the computation time in evaluating the integral of Eq. (15). In Eq. (16), $_1F_1$ represents the confluent hypergeometric function.

For the normalized mean squared displacement Eq. (12), the transformation given in Eq. (15) yields the exact anomalous behavior

$$\langle x^2(\tau)\rangle_n = \frac{2}{\Gamma(2/3)}\,\tau^{2/3} \qquad (17)$$

with $\tau \equiv (D_{2/3})^{3/2}t$ [13]. By virtue of this expression, we can approximate the anomalous diffusion constant $D_{2/3}$ as

$$D_{2/3} \approx 1.3 \times 10^{-8} \text{ m}^2/\text{s}^{2/3} \qquad (18)$$

from the experimental data plotted in Fig. 8 where the observed time interval approximately fulfills the boundary condition $C(0,\tau) = C_0$. To the best of our knowledge, this is the first time the anomalous diffusion constant appearing in the above formalism has been determined experimentally. In the following, we use $D_{2/3}$ to construct the anomalous concentration profile from Eqs. (9) and (15).

In Fig. 9, we show the anomalous concentration profile $C_\alpha(x,\tau)$ for the longest diffusion time interval ($\approx$180 h) in Fig. 7, and compare it to the Brownian profile corresponding to the same interval. The latter was combined with the diffusion constant 2×10^{-9} m^2/s (see Fig. 3). It is obvious that the subdiffusive profile lags far behind the wider spread of the Brownian counterpart, i.e., within the same time span, Brownian diffusion is more efficient. Quantitatively, this corresponds to the ratio $D_{2/3}/[D\Gamma(5/3)t^{1/3}] \approx 7.4t^{-1/3}$ s$^{1/3}$.

The subdiffusive diffusion profile sequence given in Fig. 7 is juxtaposed to the theoretical curves in Fig. 10(a). It is obvious that the general trend follows the one displayed in Fig. 7, particularly that the spacing between successive curves becomes less pronounced for increasing diffusion in-

tervals. However, it can be realized that the profile falls off too fast in comparison to the experimental result. We believe that this is related to the fact that the investigated cluster is not an ideal fractal since it is finite. This leads to corrections in the fractional model that we heuristically introduce through a fudge factor as follows. Due to the finiteness of the systems, there may exist some channels from the left to the right of the sample that enable a much faster, essentially Brownian, exchange with the reservoir.

We, therefore, propose an *ad hoc* correction, namely, we have two additive contributions, the anomalous profile plus a correction that is Brownian. That is, the resulting profile becomes

$$C(x,\tau) = C_\alpha(x,\tau_\alpha) + C_B(x,\tau_B), \qquad (19)$$

where C_α corresponds to the fractional solution with $\tau_\alpha = (D_{2/3})^{3/2}t$ (Table I) and $C_0 = 300$, and C_B is given in terms of the Brownian solution given in Eq. (9) with $\tau = Dt$ and the fudge factor amplitude $C_0 = 10$. The latter was obtained from the latest curve in Fig. 7 requiring that the value should be approximately 9 at $x = 40$ mm. This is, of course, a rough and arbitrary choice regarding the strong noise in the plot, and its purpose is only to demonstrate the difference in the profile due to this procedure.

It is obvious from Fig. 10(b) that even for the relatively small ratio $C_B(0,\tau_B):C_\alpha(0,\tau_\alpha) = \frac{1}{30}$, the profile is shifted to higher values for larger x, and that the expression given in Eq. (19) seems to be a good approximation to the experimental result. It might be argued that this measure violates the requirement that the mean squared displacement should scale proportional to $t^{2/3}$. We plotted the mean squared displacement corresponding to the modified profile, Eq. (19) in Fig. 11. It is obvious that the slope is approximately $\frac{2}{3}$, due to the small relative contribution of the Brownian solution (note that the integral determining the second moment of the Brownian contribution was cut off at $x = 80$ mm since it has a non-negligible contribution for larger x). We expect that the relative amplitude of the Brownian contribution decreases with increasing system size, i.e., the finite size effects causing the necessity of the Brownian correction should become smaller.

V. NUMERICAL EVALUATION BASED ON THE ORDINARY DIFFUSION EQUATION

In addition to the analytical propagator treatment using the fractional diffusion equation that describes the anomalous diffusion as an effective result of the complex boundary conditions, we applied numerical finite volume methods (FVM) to solve the ordinary diffusion equation (8) for the explicit boundary conditions imposed by the geometrical structure of the finite model percolation cluster. The commercial software package FLUENT 5.5™ provides the numerical basis for this sort of analysis.

The proton spin density distributions displayed in Fig. 5 were considered as a solution of the ordinary diffusion equation for the pore space of the percolation object and the initial condition of the experiment. Each lattice site is covered
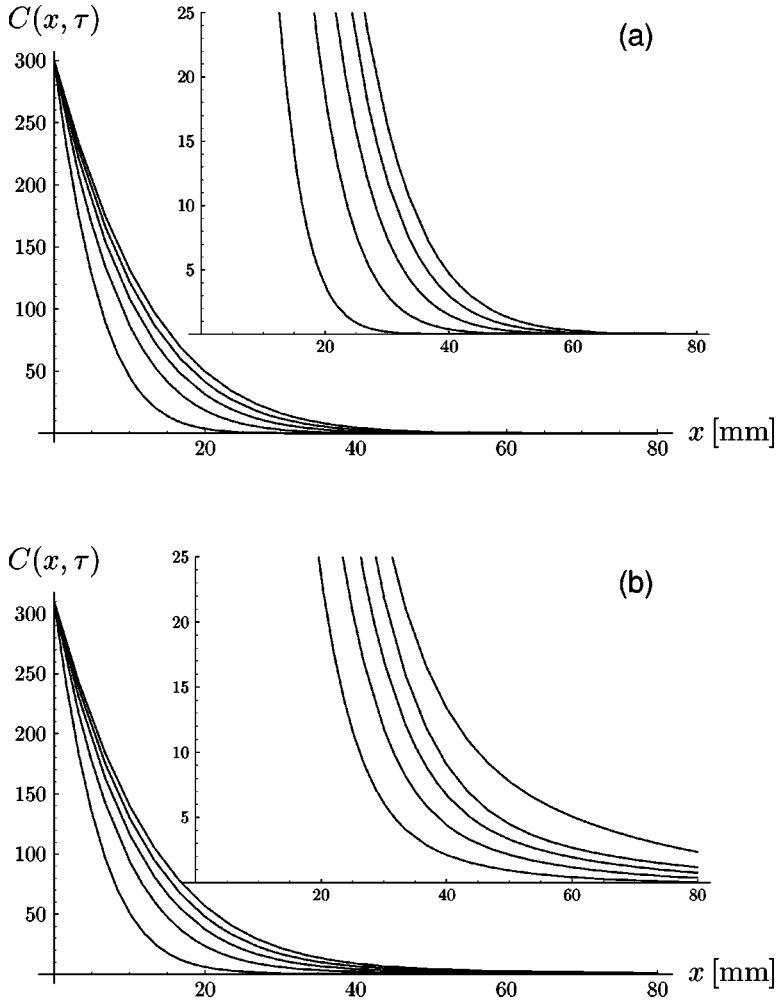
FIG. 10. (a) Anomalous concentration profile for $\alpha = \frac{2}{3}$, and with $D_{2/3} = 1.3 \times 10^{-8}$ m^2/s$^{2/3}$. The times increase away from the origin, and are taken to be 20, 60, 100, 140, and 180 h, corresponding to Fig. 7. The inset shows a zoom into the plot range [0, 25]. The conversion between t and the rescaled time τ is given in Table I. (b) Corrected anomalous concentration profile, Eq. (19), with the subdiffusive parameters $C_0 = 300$ and $D_{2/3} = 1.3 \times 10^{-8}$ m^2/s$^{2/3}$, and the Brownian diffusion constant $D = 2 \times 10^{-9}$ m^2/s. The fudge amplitude for the Brownian contribution is 10.

by a grid of 5×5 numerical unit cells. The diffusion process occurring with the ordinary diffusion constant of water at room temperature, $D = 1.8 \times 10^{-9}$ m^2/s, was treated in a series of 20 s intervals. The proton concentration at the interface to the reservoir was considered to be constant, $C(0,t) = 1$, for all times.

Figure 12 shows the normalized second moment $\langle x^2(t) \rangle_n$

evaluated from the spatial proton density distribution as a function of the time according to Eq. (12). As a consequence of the tortuous diffusion pathways in the percolation cluster, the time dependence turns out to be anomalous as expected. That is

$$\langle x^2(t) \rangle \propto t^{0.8}. \tag{20}$$

The exponent value coincides with the experimental result within the experimental accuracy, but is slightly higher than the theoretical expectation for random-site percolation clusters according to the Alexander Orbach conjecture, Eq. (3).
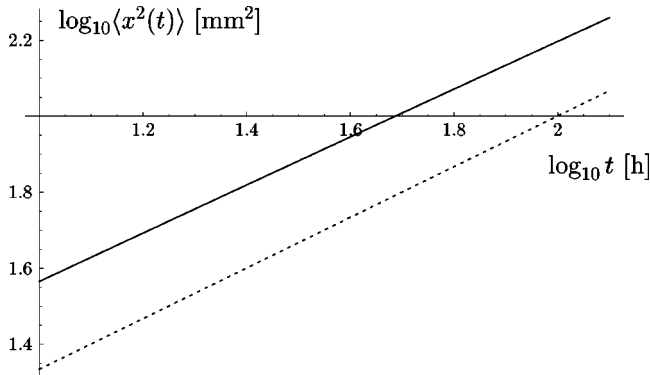

FIG. 11. Mean squared displacement corresponding to the modified profile, Eq. (19), $\log_{10}$-$\log_{10}$ scale (full line). The dashed line represents the mean squared displacement corresponding to the fractional result, Fig. 8. Both lines are approximately of slope $\frac{2}{3}$.

TABLE I. Conversion between experimental time scale and rescaled "time" $\tau = Dt$ for Brownian and anomalous case. We use $D = 2 \times 10^{-9}$ m^2/s and $D_{2/3} = 1.3 \times 10^{-8}$ m^2/s$^{2/3}$.

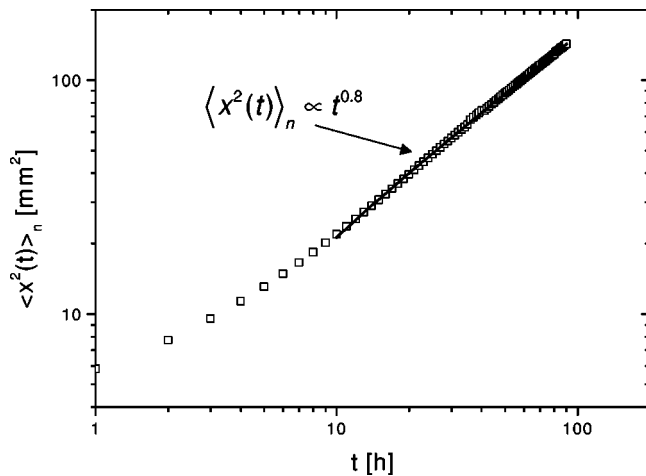| t (h)	$(D_{2/3})^{3/2} t (10^{-6}$ m$^3)$	Dt $(10^{-4}$ m$^2)$
20	0.11	1.44
60	0.33	4.32
100	0.56	7.20
140	0.78	10.10
180	1.00	12.96

FIG. 12. Time dependence of the normalized mean squared displacement evaluated from numerical solutions of the ordinary diffusion equation for the boundary conditions given by the percolation model clusters (see Fig. 5). The numerical procedure is based on FVM. The numerical transient time resolution is 20 s. The time evolution is scanned in steps of $\Delta t = 3600$ s. The data can be described by a power law $\langle x^2(t) \rangle_n \propto t^{0.8}$.

The explanation is that there is a finite contribution of undisturbed Brownian diffusion trajectories through the pore space. The channel width relative to the extension of the model system considered is not negligible as anticipated in the theoretical percolation cluster model. Therefore, a finite fraction of diffusion trajectories unaffected by the pore space restrictions contribute, and the exponent will be correspondingly larger. Of course, this ''normal'' contribution is expected to vanish in the limit of infinite system sizes.

VI. CONCLUSIONS AND DISCUSSION

In this study, we have experimentally determined fractal parameters of random-site percolation clusters based on the structural properties of the matrix, and grounded on the dy-

namic behavior of an isotopically labeled fluid filled into the pore space.

Remarkably, anomalous diffusion was found for displacements far beyond the correlation length, which is around 20 lattice constants at the occupation probabilities considered in this study (see Fig. 2). That is, the normal diffusion limit in Eq. (2) applies only extremely far above t_ξ. This finding is in accordance with recent Monte Carlo simulations [46], where the same conclusion was drawn.

Apart from the mean squared displacement considered here, it is of interest to compare the whole concentration profile with theoretical predictions. The concentration profile in principle contains all information of the (anomalous) propagator effectively determining the diffusion properties. This is shown with the analytical propagator treatment based on the fractional diffusion equation in Sec. IV. The experimental concentration profiles for water diffusion in the model percolation clusters can be described well on this basis in the sense that the qualitative behavior of the measured concentration profile can be reproduced with the solution of the fractional diffusion equation with a relatively small correction. In this way, the fractional diffusion equation formalism was verified experimentally.

Additionally, we have evaluated the ordinary diffusion equation for the boundary conditions given by the percolation model cluster. The experimental data and the propagator results obtained from the fractional diffusion equation coincide completely as far as can be judged in the frame of the accuracy of the diverse methods.

ACKNOWLEDGMENTS

[1] M. Sahimi, *Flow and Transport in Porous Media and Fractured Rock* (VCH Verlagsgesellschaft, Weinheim, 1995).

[2] A. L. Dullien, *Porous Media: Fluid Transport and Pore Structure* (Academic, New York, 1992).

[3] P. M. Adler and J.-F. Thovert, Appl. Mech. Rev. **51**, 537 (1998).

[4] D. Stauffer and A. Aharony, *Introduction to Percolation Theory* (Taylor & Francis, London, 1992).

[5] M. Sahimi, *Application of Percolation Theory* (Taylor & Francis, London, 1993).

[6] *Fractals and Disordered Systems*, edited by A. Bunde and S. Havlin (Springer-Verlag, Berlin, 1996).

[7] R. Orbach, Science **231**, 814 (1986).

[8] P. Levitz, Europhys. Lett. **39**, 593 (1997).

[9] S. Havlin and D. Ben-Avraham, Adv. Phys. **36**, 695 (1987).

[10] F. Klammler and R. Kimmich, Croat. Chem. Acta **65**, 455 (1992).

[11] R. Kimmich, F. Klammler, V. D. Skirda, I. A. Serebrennikova, A. I. Maklakov, and N. Fatkullin, Appl. Magn. Reson. **4**, 425 (1993).

[12] R. Kimmich, S. Stapf, R.-O. Seitter, P. Callaghan, and E. Khozina, in *Dynamics in Small Confining Sytems*, edited by J. M. Dyake *et al.*, Mater. Res. Soc. Symp. Proc. No. **366** (Materials Research Society, Pittsburgh, 1995), 189.

[13] R. Metzler and J. Klafter, Phys. Rep. **339**, 1 (2000).

[14] H.-P. Müller, J. Weis, and R. Kimmich, Phys. Rev. E **52**, 5195 (1995).

[15] H.-P. Müller, R. Kimmich, and J. Weis, Phys. Rev. E **54**, 5278 (1996).

[16] A. Klemm, H.-P. Müller, and R. Kimmich, Phys. Rev. E **55**, 4413 (1997).

[17] A. Klemm, R. Kimmich, and M. Weber, Phys. Rev. E **63**, 041514 (2001).

[18] H. Hermann, *Stochastic Models of Heterogeneous Materials*

(Trans Tech Publications, Zürich, 1991).

[19] A. Kapitulnik, A. Aharony, G. Deutscher, and D. Stauffer, J. Phys. A **16**, L269 (1983).

[20] S. Alexander and R. Orbach, J. Phys. (France) Lett. **43**, L-625 (1982).

[21] D. C. Hong, S. Havlin, H. J. Herrmann, and H. E. Stanley, Phys. Rev. B **30**, 4083 (1984).

[22] J. G. Zabolitzky, Phys. Rev. B **30**, 4077 (1984).

[23] W. R. Schneider and W. Wyss, J. Math. Phys. **30**, 134 (1989).

[24] R. Kimmich, *NMR Tomography, Diffusometry, Relaxometry* (Springer-Verlag, Berlin, 1997).

[25] P. T. Callaghan, *Principles of NMR Microscopy* (Clarendon Press, Oxford, 1991).

[26] V. Pasquier, P. Levitz, and A. Delville, J. Phys. Chem. **100**, 10249 (1996).

[27] R. W. Mair, G. P. Wong, D. Hoffmann, M. D. Hürlimann, S. Patz, L. M. Schwartz, and R. L. Walsworth, Phys. Rev. Lett. **83**, 3324 (1999).

[28] M. J. Lizak and M. S. Conradi, J. Magn. Reson. (1969-1992) **95**, 548 (1991).

[29] D. O. Kuethe, A. Caprihan, E. Fukushima, and R. A. Waggoner, Magn. Reson. Med. **39**, 85 (1998).

[30] W. Heink, J. Kärger, and H. Pfeifer, Chem. Eng. Sci. **33**, 1019 (1978).

[31] R. Kimmich, G. Schnur, and M. Köpf, Prog. Nucl. Magn. Res. Spectrosc. **20**, 385 (1988).

[32] A. Klemm, H.-P. Müller, and R. Kimmich, Physica A **266**, 242 (1999).

[33] B. M. Fung, Biophys. J. **18**, 235 (1977).

[34] N. Jan, Physica A **266**, 72 (1999).

[35] R. Mills, J. Phys. Chem. **77**, 685 (1973).

[36] J. Crank, *The Mathematics of Diffusion* (Clarendon Press, Oxford, 1975).

[37] M. Holz and H. Weingärtner, J. Magn. Reson. **92**, 115 (1991).

[38] P. Lévy, *Processus Stochastiques et Mouvement Brownien* (Gauthier-Villars, Paris, 1965); W. Feller, *An Introduction to Probability Theory and Its Applications* (Wiley, New York, 1968), Vol. 2.

[39] J.-P. Bouchaud and A. Georges, Phys. Rep. **195**, 127 (1990).

[40] We note that D_α is connected with the generalized friction constant η_α through the generalized Einstein-Stokes relation $D_\alpha = k_B T/(m\eta_\alpha)$ [13]. This relation could be observed experimentally [41] and the use of D_α therefore has a similar physical meaning as the traditional diffusion constant D in Brownian motion.

[41] E. Barkai and J. Klafter, Phys. Rev. Lett. **81**, 1134 (1998); F. Amblard, A. C. Maggs, B. Yurke, A. N. Pargellis, and S. Leibler, *ibid.* **81**, 1135 (1998); **77**, 4470 (1996).

[42] J. Klafter, A. Blumen, and M. F. Shlesinger, Phys. Rev. A **35**, 3081 (1987); J. Klafter, G. Zumofen, and A. Blumen, J. Phys. A **25**, 4835 (1991); J. Klafter, M. F. Shlesinger, and G. Zumofen, Phys. Today **49**, 33 (1996).

[43] K. B. Oldham and J. Spanier, *The Fractional Calculus* (Academic, New York, 1974).

[44] R. Metzler and J. Klafter, J. Phys. Chem. B **104**, 3851 (2000); Phys. Rev. E **61**, 6308 (2000); R. Metzler, *ibid.* **62**, 6233 (2000).

[45] E. Barkai and R. Silbey, J. Phys. Chem. B **104**, 3866 (2000).

[46] O. J. Poole and D. W. Salt, J. Phys. A **29**, 7959 (1996).